

Extended OVI haloes of starforming galaxies

Evgenii O. Vasiliev^{1,2*}, Marina V. Ryabova^{2†}, Yuri A. Shchekinov^{2,3‡}

¹*Institute of Physics, Southern Federal University, Stachki Ave. 194, Rostov-on-Don, 344090 Russia*

²*Department of Physics, Southern Federal University, Sorge Str. 5, Rostov-on-Don, 344090 Russia*

³*Isaac Newton Institute of Chile, SAO Branch*

Accepted 3004 December 15. Received 2004 December 14; in original form 2004 December 31

ABSTRACT

We consider evolution of metal-enriched gas exposed to a superposition of time-dependent radiation field of a nearby starburst galaxy and nearly invariant (on timescales 100 Myr) extragalactic ionization background. Within nonequilibrium (time-dependent) photoionization models we determine ionization fraction of the OVI ion commonly observed in galactic circumference. We derive then conditions for OVI to appear in absorptions in extended galactic haloes depending on the galactic mass and star formation rate. We have found that the maximum OVI fraction can reach $\sim 0.4 - 0.9$ under combined action of the galactic and the extragalactic ionizing radiation fields. We conclude that soft X-ray emission with $E \gtrsim 113$ eV from the stellar population of central starforming galaxies is the main source of such a high fraction of OVI. This circumstance can explain high column densities $N(\text{OVI}) \sim 10^{14.5-15.3} \text{ cm}^{-2}$ observed in the haloes of starforming galaxies at low redshifts (Tumlinson et al. 2011) *even* for a relatively low ($\sim 0.01 - 0.1 Z_{\odot}$) metallicity. As a result, the requirements to the sources of oxygen in the extended haloes relax to a reasonably conservative level. We show that at $z \lesssim 0.5$ ionization kinetics of oxygen in a relatively dense plasma $n \gtrsim 10^{-4} \text{ cm}^{-3}$ of outer halo exposed to a low extragalactic ionizing flux is dominated by nonequilibrium effects.

Key words: galaxies: evolution – haloes – starburst – theory – diffuse radiation – intergalactic medium – quasars: general – absorption lines – physical data and processes: atomic processes

1 INTRODUCTION

Strong OVI absorptions observed around starforming galaxies at $z \sim 0.1 - 0.4$ with impact parameter as high as 150 kpc reveal huge gaseous galactic haloes (Tumlinson et al. 2011). Even conservative estimates lead to amount of gas in them far exceeding the gas reservoir in galaxies themselves. Such a conclusion is based on the assumption that gas in the haloes has solar metallicity. The arguments underlying this assumption stem from the standard estimate of oxygen mass from the observed column density (Tumlinson et al. 2011)

$$M_{\text{O}} = 5\pi R^2 \langle N_{\text{OVI}} \rangle m_{\text{O}} f_{\text{hit}} \left(\frac{0.2}{f_{\text{OVI}}} \right) = 1.2 \times 10^7 \left(\frac{0.2}{f_{\text{OVI}}} \right) M_{\odot}, \quad (1)$$

where a typical column density $\langle N_{\text{OVI}} \rangle = 3 \times 10^{14} \text{ cm}^{-2}$,

the halo radius $R = 150$ kpc, the hit rate correction factor (covering factor) $f_{\text{hit}} = 0.8 - 1$ are assumed following by Tumlinson et al. (2011), $m_{\text{O}} = 16m_{\text{H}}$ is atomic mass of oxygen. The fractional abundance of OVI under thermal collisional ionization equilibrium never exceeds $f_{\text{OVI}} = 0.2$ (e.g. Ferland et al. 1998; Gnat & Sternberg 2007), such that within this assumption Eq. (1) provides a lower estimate of oxygen mass in the halo (Tumlinson et al. 2011). It is readily seen from here that the mass $M_{\text{O}} \sim 10^7 M_{\odot}$, i.e. around 10 to 70% of oxygen mass in the ISM, is indeed a conservative estimate.

In principle, this conclusion for galactic haloes to bear such a large gas mass would might solve the problem of missing baryons and metals (Bregman et al. 2009; Pettini 1999), though requiring enormously high oxygen production and mass ejection rates. Moreover, the fraction $f_{\text{OVI}} = 0.2$ under collisional ionization equilibrium is kept only in a very narrow temperature range: $T = (3 - 5) \times 10^5$ K (e.g. Ferland et al. 1998; Gnat & Sternberg 2007). It is therefore totally unrealistic to assume that all observed haloes keep

* E-mail: eugstar@mail.ru

† E-mail: mryabova@sfnu.ru

‡ E-mail: yus@sfnu.ru

their temperatures within such a narrow range independent on distance from the host galaxy.

In their estimates Tumlinson et al. (2011) used the ionic fractions calculated under collisional and/or photoionization equilibrium conditions, i.e. independent of time (Ferland et al. 1998). However, ionization state of gas situated in time-dependent (nonequilibrium) environment can differ qualitatively from the one settled on to equilibrium, particularly, for solar metallicity (Vasiliev 2011). This difference can be smaller for low-density gas exposed to a strong ionizing field. However, in the process of galactic evolution both the magnitude and the shape of the radiation spectrum can change. In addition the extragalactic spectrum, which can be important on the periphery of galactic haloes, does also evolve (Haardt & Madau 2001; Faucher-Giguère et al. 2009). Under such conditions it is natural to expect the ionic composition to experience time variations.

In this paper we therefore concentrate on the question of whether evolution of the ionizing radiation field can result in considerable changes of fractional ionization of oxygen such to make estimates of gas mass in galactic haloes more reliable. In next sections we will demonstrate that indeed under time-dependent conditions the observed column densities of OVI correspond to at least half order of magnitude less massive haloes, which can stay in a much wider range of physical parameters.

The paper is organized as follows. In Section 2 we describe the details of the model. In Section 3 we present our results. Section 4 summarizes the results.

2 MODEL DESCRIPTION

Thermal and ionization state in our model is fully time-dependent: the model involves ionization and thermal evolution of gas located at radii $\sim 50 - 300$ kpc in the galactic halo, exposed to extragalactic and galactic time-dependent ionizing radiation field.

2.1 Time-dependent ionization

In this paper we only briefly touch main features of calculation of the ionization and thermal evolution of gas immersed into external time-dependent ionizing radiation. The details can be found in (Vasiliev 2011). We study ionization and thermal evolution of a lagrangian gas element: a gas parcel is assumed to be optically thin to external ionizing radiation. In the calculations we include all ionization states of the elements H, He, C, N, O, Ne, Mg, Si and Fe. We take into account the following major processes: photoionization, multi-electron Auger ionization process, collisional ionization, radiative and dielectronic recombination, collisional excitation as well as charge transfer in collisions with hydrogen and helium atoms and ions.

The total cooling and heating rates are calculated using as a subroutine the photoionization code CLOUDY (ver. 10.00, Ferland et al. 1998). More specifically, we input into CLOUDY code a given set of all ionic fractions X_i calculated at temperature T , gas density n and external ionization flux $J(\nu)$ and obtain the corresponding cooling and heating rates. The latter also includes Compton heating from X-rays. For the solar metallicity we adopt the abundances reported by

Asplund et al. (2005), except Ne for which the enhanced abundance is adopted (Drake & Testa 2005). In all calculations we assume the helium mass fraction $Y_{\text{He}} = 0.24$, which corresponds to $[\text{He}/\text{H}] = 0.081$, and is close to the observed one (Izotov & Thuan 1998).

We solve a set of 96 coupled equations (95 for ionization states and one for temperature) using a Variable-coefficient Ordinary Differential Equation solver (Brown et al. 1989). We considered the two regimes of gas evolution: isochoric and isobaric. The isochoric regime suggests that gas density in a cloud is kept constant, while in isobaric model gas pressure is assumed constant. The two regimes correspond to two opposite limits of the ratio between the cooling and the sound crossing times: $t_c = kT/\Lambda n$ and $t_s = R/c_s$, correspondingly. In the external heating radiation field isobaric models show essentially similar thermal and ionization evolution, though on longer time scales due to decreasing density coupled to increasing temperature. It results in an increase of the cross-section of gas clouds such that their covering factor increases as well.

2.2 Galaxy evolution

In the process of galaxy evolution the stellar content changes: massive stars produce enormous number of UV photons and form ultimately compact objects which emit hard ionizing photons. Spectrum of the ionizing radiation escaping galactic interstellar medium (ISM) and exposing further the halo depends on amount of metals in the ISM disk absorbing ionizing photons, and thus on chemical evolution of the galaxy. In order to follow evolution of stellar mass, metallicity and galaxy spectrum, we use the spectro-photometric code PEGASE (Fioc & Rocca-Volmerange 1997). We assume a Schmidt-like power-law starformation rate (SFR): $\text{SFR}(t) = \mathcal{M}_g^{p_1}/p_2$, typical SFR for massive starforming galaxies, where \mathcal{M} is the normalized mass of gas in M_\odot . In some regions of the galaxy SFR can be inhibited by gas outflows from the disk, however, when averaged over the whole disk the SFR remains sufficiently high over the whole period of active star formation. In our models we assumed a closed-box regime. In general, though this cannot be applied to galaxies with active star formation. However, many parameters related to mass and energy exchange between galaxies and the intergalactic medium, such as the rates of mass ejection from and mass accretion from the ambient medium, gas metallicity and corresponding cooling rate, clustering of SNe explosions, etc are highly uncertain and hard to be coherently described phenomenologically.

2.3 Time-dependent UV/X-ray backgrounds

Gas in galactic haloes is exposed by a cumulative ionizing background consisting of the extragalactic and the galactic components. The extragalactic component is uniform on galactic halo scales, and is nearly constant on timescales ~ 100 Myr, while changes significantly on longer times. For the extragalactic background we accept the spectrum described by Haardt & Madau (2001). Its evolution covers redshifts $z = 0$ to $z = 9$ divided by 49 equally spaced log bins. Contribution from possible flux sources varies over cosmological time, and irregular changes in different bands of the

spectrum with redshift can be met. For this reason simple linear approximation between neighbour redshift bins was used.

The galactic component instead, may change on much shorter timescales. In general, the corresponding time scale is close to the lifetime of massive stars, i.e. $\sim 10 - 20$ Myr. This galactic radiation component originates in the central star forming region, and is seen from outer parts of the halo at distances $\gtrsim 30 - 50$ kpc as a nearly spherical domain of size of $\sim 2 - 3$ kpc.

The ionizing radiation from stellar population is partly modified by absorption in the interstellar medium of underlying bulge and disk. In order to account this absorption we assume that ionizing photons pass through a layer of neutral gas in galactic disc with the optical depth $\tau_\nu = \sigma_\nu^{\text{HI}} N_{\text{HI}} + \sigma_\nu^{\text{HeI}} N_{\text{HeI}}$, throughout the paper $N_{\text{HI}} = 10^{20} \text{ cm}^{-2}$, $N_{\text{HeI}} = 10^{19} \text{ cm}^{-2}$ are considered as fiducial. The corresponding optical depths at the HI and HeI Lyman limits are as high as ~ 630 and 70 , respectively. As a result only photons with $E \gtrsim 60$ eV escape the galaxy and penetrate into halo; the ionizing flux with photons of $E > 60$ eV decreases as r^{-2} . In what follows we will discuss the dependence of our results on the HI column density.

In our model the galactic UV spectrum is calculated with making use the PEGASE code (Fioc & Rocca-Volmerange 1997), which gives spectral luminosity in the range from 91\AA to $160 \mu\text{m}$. In order to extend the spectrum to higher energies (up to $\sim 10^4$ eV, responsible for ionization of highly charged ionic species) we use the empirical relation ‘ $L_X - SFR$ ’ (Gilfanov et al. 2004). This relation is well established for massive starforming galaxies considered here.

Overall the cumulative spectrum varies on time scales from several to hundreds of millions years.

2.4 Initial set up

We consider gas in outer haloes of massive (Milky Way type) starforming galaxies with stellar mass of several $\times 10^{10} M_\odot$. Recent simulations of the Milky Way halo show that it extends up to the virial radius of the Milky Way (i.e., $\sim 50 - 300$ kpc) with densities ranging within $\sim (0.5 - 2) \times 10^{-4} \text{ cm}^{-3}$ (Feldmann et al. 2013). Observational estimates of the circumgalactic gas density around the Milky Way and other Local Group galaxies give similar numbers $\sim (1 - 3) \times 10^{-4} \text{ cm}^{-3}$ at $r \sim 40 - 150$ kpc (Weiner & Williams 1996; Grcevich & Putman 2009; Quilis & Moore 2001; Stanimirović et al. 2002; Anderson & Bregman 2010). In our calculations we follow these numbers and set $n = (0.5 - 2) \times 10^{-4} \text{ cm}^{-3}$ in the circumgalactic volume. We consider both isochoric and isobaric regimes.

We start the calculations at $z = 2$ (the lookback time is around 10 Gyrs). This timescale is nearly the cooling time for hot gas with $T \sim 10^6$ K and $\sim (0.5 - 2) \times 10^{-4} \text{ cm}^{-3}$ (Feldmann et al. 2013). The last major merging for Milky Way-type galaxies is thought to occur earlier than $z \sim 2$ (e.g., Hammer et al. 2007).

The initial ionic composition and the temperature are set equal to the ones corresponding to photoequilibrium in gas exposed to the extragalactic Haardt & Madau spectrum at $z = 2$. Such radiation field is sufficient to force low den-

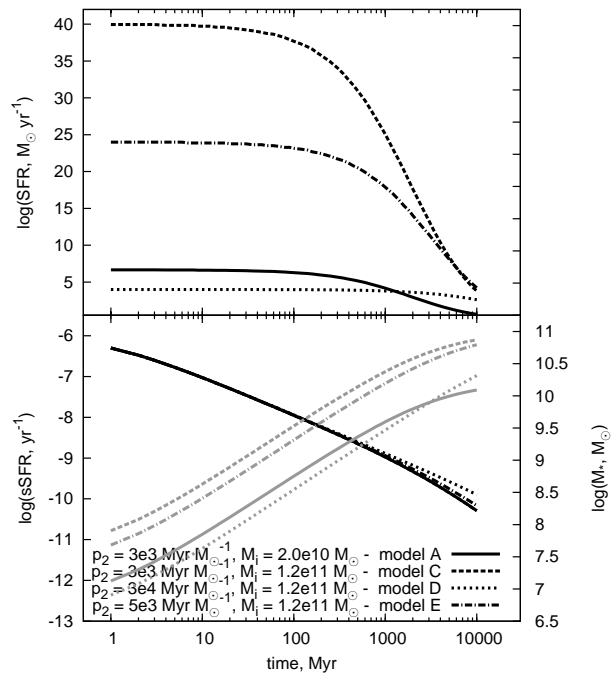


Figure 1. *Upper panel:* the star formation rate. *Lower panel:* the specific star formation rate, $s\text{SFR} = \text{SFR}/M_*$ (solid black), and the stellar mass, M_* (solid grey); the initial time corresponds to $z = 2$. The four models with the rate $\text{SFR}(t) = \mathcal{M}^2/p_2$ are shown: two models with fixed $p_2 = 3 \times 10^3 \text{ Myr } M_\odot^{-1}$ and the initial gaseous mass $M_g^i = 2 \times 10^{10} M_\odot$ (model A – solid line), and $M_g^i = 1.2 \times 10^{11} M_\odot$ (model C – dashed line). The other two models are with fixed $M_g^i = 1.2 \times 10^{11} M_\odot$ and different $p_2 = 3 \times 10^4 \text{ Myr } M_\odot^{-1}$ (model D – dotted line), and $p_2 = 5 \times 10^3 \text{ Myr } M_\odot^{-1}$ (model E – dash-dotted line).

sity gas with n in the accepted range to settle quickly onto photoequilibrium (Vasiliev 2011). Calculations cover physical time scales much longer than the relaxation time scale of ionization and thermal processes in gas exposed to the time-dependent spectrum adopted here.

Gas metallicity in our models is assumed to range within 10^{-2} to $0.1 Z_\odot$. Higher metallicities are rare in DLA QSO and DLA GRB absorbers (Savaglio 2009). The lower limit lies around ten times above the upper limit of the IGM metallicity at $z \sim 2 - 3$ (e.g., Cowie et al. 1995; D’Odorico et al. 2010).

3 RESULTS

3.1 SFR and spectral evolution

From the chemical evolution models calculated with the PEGASE code we obtain the time-dependent starformation rate, stellar mass, gas metallicity and spectral luminosity. We simulated several models corresponding to massive galaxies and chose two of them, whose parameters, namely the SFR and the stellar mass, are close to those of the starforming galaxies described by Tumlinson et al. (2011). With the accepted SFR law $\text{SFR}(t) = \mathcal{M}^{p_1}/p_2$, where \mathcal{M} is the normalized mass of gas in M_\odot and through the paper $p_1 = 2$ is assumed, the notations are as in

(Fioc & Rocca-Volmerange 1997). In total we consider four models. The first two suggest a fixed normalization factor $p_2 = 3 \times 10^3 \text{ Myr } M_\odot^{-1}$, and two different values of the initial gaseous mass: $M_g^i = 2 \times 10^{10} M_\odot$ – model A, and $M_g^i = 1.2 \times 10^{11} M_\odot$ – model C. The other two models assume a fixed initial gaseous mass $M_g^i = 1.2 \times 10^{11} M_\odot$, and two different normalization constants p_2 : one with $p_2 = 3 \times 10^4 \text{ Myr } M_\odot^{-1}$ – model D, and the other with $p_2 = 5 \times 10^3 \text{ Myr } M_\odot^{-1}$ – model E.

Figure 1 presents the star formation rate, SFR, the specific starformation rate, $\text{sSFR} = \text{SFR}/M_*$, and the stellar mass, M_* : model A (solid line), model C (dashed line), model D (dotted line) and model E (dash-dotted line). Two features are to note: first, the sSFR reveals differences between the models only after several hundreds of Myrs, and second, models A and C show practically equal sSFR, and as a result gas in these models is equally converted into stars by $\sim 10 \text{ Gyr}$. Instead, model D ($p_2 = 3 \times 10^4 \text{ Myr } M_\odot^{-1}$) leaves the galaxies gas-rich – only $\sim 20 \%$ of gaseous mass exhausts by this time. The characteristic time for the gas to exhaust is $t_g \sim p_2/M_g$, which gives $t_g \gtrsim 300 \text{ Myr}$ for all considered models, resulting in a nearly constant SFR (upper panel in Figure 1) over first 200 Myr with the $\text{SFR} \propto p_2^{-1}$, and decreasing on later times as $\text{SFR} \propto p_2/t^2$.

Figure 2 shows the dependence of specific starformation rate on the stellar mass for the models A (pentagons), C (circles), D (up-triangles) and E (down-triangles). Filled large symbols mark time moments shown nearby. Data for the starforming and passive galaxies studied by Tumlinson et al. (2011) are depicted by small squares and rhombs, correspondingly. The grey-scale map shows SDSS+GALEX galaxies (Schiminovich et al. 2007). It is readily seen that almost all points for the starforming galaxies are locked between tracks of the models considered here. One can expect therefore that spectral properties of starforming galaxies from Tumlinson et al. (2011) are similar to those in the models A and C during the latest $\sim 3\text{-}4 \text{ Gyrs}$ of their evolution. Passive galaxies have an order of magnitude lower sSFR.

Dash-dotted line in Figure 3 shows the galactic spectral luminosity at $t = 7.5 \text{ Gyr}$, which is equal time elapsed from $z = 2$ to 0.2. A significant break is clearly seen at the wavelength 91 \AA , which corresponds to the minimum wavelength in the spectrum reached in the PEGASE code¹. The break is due to an exponential decrease of the number of such hard photons emitted by stellar population (see e.g. Rauch 2003), as they are only produced by very massive

¹ The cut at 91 \AA in the galactic spectral energy distribution (SED) generated by the stellar population codes (e.g. PEGASE, Starburst99, Galaxev) is apparently due to a choice of the developers and might be partly connected with the availability of spectral data in stellar libraries. The stellar library calculated by Rauch (2003) contains spectra up to 1 \AA is not included yet into stellar population codes. It is worth also noting in this connection considerable deviations of the spectral distribution above 228 \AA predicted by different stellar population codes (Kewley et al. 2001). In this sense our conclusions may depend on our choice of the stellar population code and, particularly, on the cut at 91 \AA . In Section 3.3 we discuss stability of our results against possible variations of the galactic SED, and influence of the cut at 91 \AA on the ionization and thermal evolution of the circumgalactic gas.

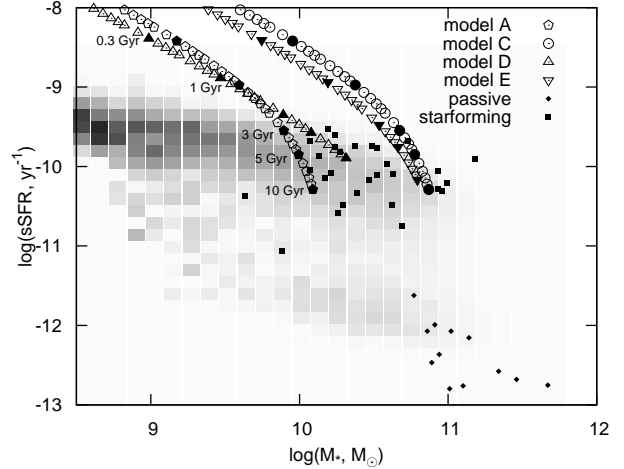


Figure 2. The dependence of the specific starformation rate on the stellar mass for models A (pentagons), C (circles), D (up-triangles) and E (down-triangles). Filled large symbols mark time moments indicated in the Figure. Data for the starforming and passive galaxies from Tumlinson et al. (2011) are depicted by small squares and rhombs, correspondingly. The grey-scale map is for SDSS+GALEX galaxies (Schiminovich et al. 2007). SFR models are described in text and Figure 1.

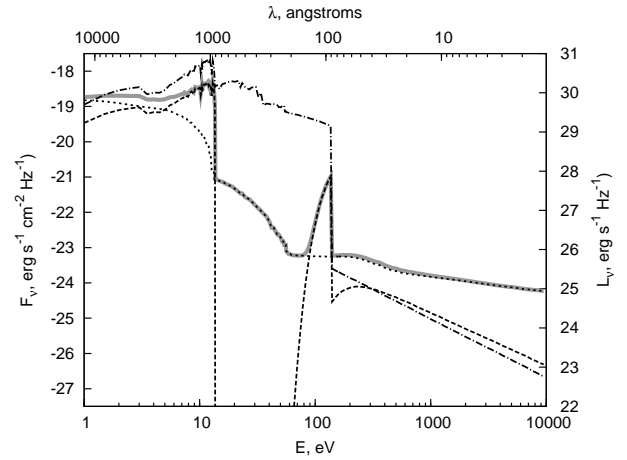


Figure 3. The cumulative ionizing background flux (thick grey line) at $z = 0.2$ and a distance from the galaxy $d = 100 \text{ kpc}$, which consists of the UV and X-ray galactic spectrum, attenuated by galactic neutral gas (dash line), the extragalactic ionizing background (dotted line). The galactic spectral luminosity is shown by dash-dotted line (the right axis).

stars, whose number is very small. As soon as we consider galactic evolution on timescales longer than $1\text{-}3 \text{ Gyr}$ X-ray binaries are expected to have already formed, and we extend the spectrum to higher energies assuming the empirical relation between X-ray luminosity and star-formation rate “ $L_X - \text{SFR}$ ” (Gilfanov et al. 2004).

By the thick grey line Figure 3 shows also an example of the total spectral radiation flux exposing a given gas parcel located at distance $d = 100 \text{ kpc}$ from the galaxy evolved till $z = 0.2$. The total spectrum consists of the galactic (dash line) and extragalactic (dotted line) ionizing photons. At low energies, $E \lesssim 13.6 \text{ eV}$, the extragalactic contribution dominates at large distances, $d \gtrsim 100 \text{ kpc}$, while the stel-

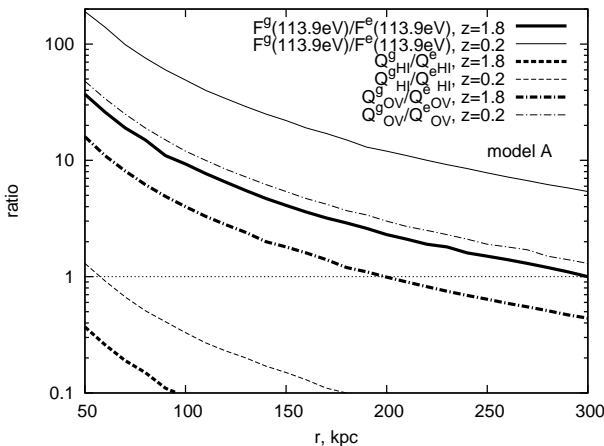


Figure 4. The ratio of monochromatic galactic flux to the extragalactic one at 113.9 eV (solid lines), and the ratios of ionizing photon number fluxes $Q_{\text{HI}}^g/Q_{\text{HI}}^e$ (dash lines) and $Q_{\text{OV}}^g/Q_{\text{OV}}^e$ (dash-dotted lines), where the superscripts ‘g’ and ‘e’ refer to galactic and extragalactic backgrounds. Thick and thin lines correspond to redshifts 1.8 and 0.2, respectively.

lar population turns into play in UV range at smaller distances. Strong absorption of the galactic ionizing photons ($E \sim 13.6 - 90$ eV) in the galactic disk with the fiducial N_{HI} and N_{HeI} values results in the total dependence of the ionic composition of halo gas on the extragalactic background. The significance of absorption by the galactic disk can be understood from comparison of the galactic spectral luminosity shown by dash-dotted line and the cumulative flux (thick grey line).

A narrow bump at $E \sim 90 - 136$ eV is due to the galactic photons survived against absorption in thick disk. Its magnitude is obviously determined by our choice of the neutral column densities N_{HI} and N_{HeI} in the disk. For the fiducial values of N_{HI} and N_{HeI} the optical depth is about 3 for photons with $E \sim 113$ eV. Higher column densities can erase the bump and the extragalactic flux becomes dominating in the whole galactic halo. Decrease of the galactic contribution is also seen at larger distances from the galaxy due to dilution r^{-2} . Note that the ionization potential of OV, $I_{\text{OV}} = 113.9$ eV falls exactly in this the range $E \sim 90 - 136$ eV. This means that the fraction of OVI ions can increase in galaxies with lower column densities (N_{HI} and N_{HeI}) in their disks.

In general, the excess of galactic photons with energies higher than 113.9 eV contributes crucially into ionization kinetics of OVI ion. Figure 4 presents the ratio of monochromatic galactic and extragalactic fluxes at 113.9 eV (solid lines) in model A for our fiducial column densities N_{HI} and N_{HeI} . It is clearly seen that the galactic flux dominates within $r \lesssim 300$ kpc at redshifts $z > 0.2$. At lower redshifts the region of predominance of galactic flux widens mostly due to a step decrease of the extragalactic flux in these epochs. The monochromatic radiation at the HI Lyman limit is fully absorbed in the disk for the fiducial N_{HI} and N_{HeI} column densities.

In order to estimate both the escape of HI ionizing photons and the efficiency of OV ionization we calculate radial dependences of the ratios of ionizing fluxes $Q_{\text{HI}}^g/Q_{\text{HI}}^e$ and $Q_{\text{OV}}^g/Q_{\text{OV}}^e$, where the superscripts ‘g’ and ‘e’ refer to

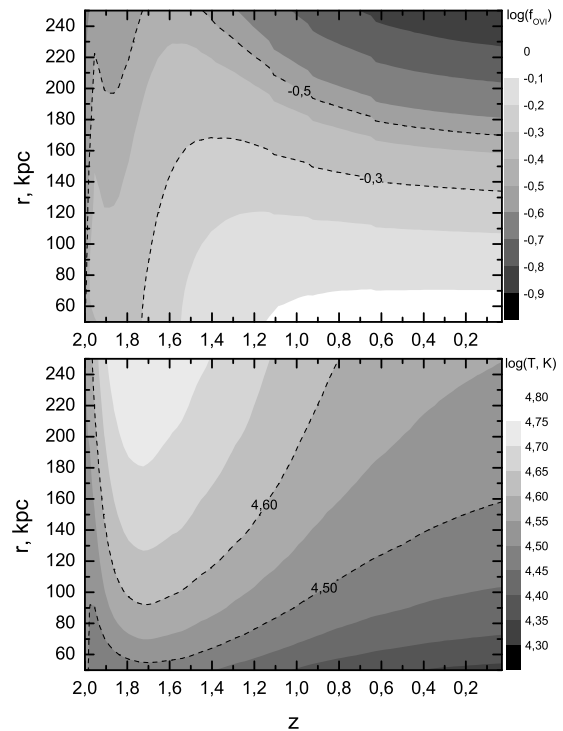


Figure 5. The temperature (lower panel) and OVI fraction (upper panel) evolution (dependence on redshift) of a gas at different distances from the galactic center. We assume the SFR as that in model A and our fiducial values of N_{HI} and N_{HeI} .

the galactic and extragalactic contributions. Figure 4 shows these ratios at $z = 1.8$ and 0.2 for model A. In the energy range $E \gtrsim 113.9$ eV the galactic contribution dominates up to distance $r \lesssim 200$ kpc at $z = 1.8$, and extends even to $r \lesssim 300$ kpc at $z = 0.2$ due to strong decrease of the extragalactic background at low redshifts. It is obvious, that increase of ionizing flux enlarges radius of the zone of predominance of galactic ionizing photons: for instance, this zone increases from ~ 200 kpc in model A to ~ 300 kpc in model C at $z = 1.8$. Decrease of absorption in the disk does also promote the zone of the galactic predominance to grow: it reaches $r \gtrsim 250$ kpc for $N_{\text{HI}} \lesssim 10^{19} \text{ cm}^{-2}$ even in model A.

3.2 Thermal and ionization evolution

Figure 5 shows evolution of temperature (lower panel) and OVI fraction (upper panel) in gas located at different distances from the galactic center; here we assume the SFR as in model A and our fiducial column densities N_{HI} and N_{HeI} .

In the beginning, $z \sim 2$, oxygen is mainly locked in the OVII state due to high ionizing flux. Its fraction establishes around ~ 0.5 under the influence of the extragalactic ionizing background. After several hundreds million years the extragalactic background starts decreasing following the cosmic star formation rate. It should result in a quick transition from OVII to OVI. In a cooling plasma OVI recombines rapidly into lower ionization states and practically disappears shortly – a well-known OVI “fragility”. However, in

our case the excess of photons with $E > I_{\text{OVI}} = 113.9$ eV emitted by starforming galaxies does not allow OVI to recombine. Consequently, its fraction remains almost frozen at the level ~ 0.5 in the region $d \lesssim 300$ kpc over the range $z \sim 1.2$ till 0. In our models $f(\text{OVI})$ reaches $\sim 0.4 - 0.9$ in a low-metallicity ($0.1 Z_{\odot}$) gas within $50 < d < 150$ kpc from $z \sim 1$ to 0. This value is several times higher than the maximum OVI fraction, $\sim 0.1 - 0.2$, reached in gas exposed only to the extragalactic background (e.g. Ferland et al. 1998; Gnat & Sternberg 2007), and in nonequilibrium collisional gas evolved from $T = 10^8$ K (see e.g. Gnat & Sternberg 2007). Note that even at large distances $d \sim 250$ kpc $f(\text{OVI})$ remains higher than 0.1. The temperature of gas with such high OVI fraction is within $(2-5) \times 10^4$ K (see lower panel in Figure 5). The dependence of $f(\text{OVI})$ on metallicity is weak: for instance, OVI fraction in gas with $0.01 Z_{\odot}$ is $\sim 0.1 - 0.8$ within distances $50 < d < 300$ kpc in model A.

Cooling of gas with $Z \lesssim 0.1 Z_{\odot}$ exposed only to the extragalactic background is mainly due to hydrogen and helium, whereas metals (oxygen and carbon) play a minor role in radiation losses (e.g. Wiersma et al. 2009; Vasiliev 2011). A considerable increase of OVI fraction in the zones where galactic ionization dominates enhances the contribution of oxygen into cooling. As a result, gas temperature is lower in these regions as seen on the lower panel in Figure 5.

Deviation of column densities from the fiducial values accepted above may result in a considerable change of the overall picture due to changes of the interrelation between the fractions of galactic and extragalactic ionizing photons. In order to understand how sensitive is the oxygen ionization state to surface density of the underlying galactic gaseous discs we calculate several models with different N_{HI} and N_{HeI} . For simplicity we assume that $N_{\text{HI}}/N_{\text{HeI}} = 10$.

Figure 6 presents the galactic part of the spectrum at distance $d = 100$ kpc and redshift $z = 0.1$ for several values N_{HI} (upper panel), and the evolution of OVI fraction in gas exposed to this radiation field (lower panel). For column density $N_{\text{HI}} = 10^{20} \text{ cm}^{-2}$ the galactic spectrum in model A is fully absorbed in the range 13.6-80 eV. Only for a hundredth of this column density the attenuation becomes less depressing. A lower column density $N_{\text{HI}} \lesssim 10^{19} \text{ cm}^{-2}$ allows a higher fraction of ionizing photons with the energy above the ionization potential of OV (113 eV) to penetrate into the halo and support a higher fraction of OVI (lower panel): the OVI fraction reaches $\sim 0.8 - 0.9$ and slightly increases for lower column densities. This value is considerably higher than in collisionally ionized gas and in gas photoionized only by the extragalactic background. The reason for such a high fraction of OVI is in the break at the energy slightly lower than the OVI ionization potential (136 eV). It is worth noting that the uncertainty of the spectral energy distribution in this energy range within stellar population codes is rather high. This partly stems from the stellar atmosphere models and the rarity of extremely massive stars (Rauch 2003). On one hand this is a shortcoming of our model, though on the other, the rarity of massive stars and their short lifetime allows us to think that stellar contribution into circumgalactic ionizing field falls steeply down at energies $E \gtrsim 125 - 130$ eV (see the spectra of the hottest stars in Rauch 2003), which is lower than the OVI ionization potential (136 eV). However it is important to note that the predominance of galactic flux over the extragalactic background in the range

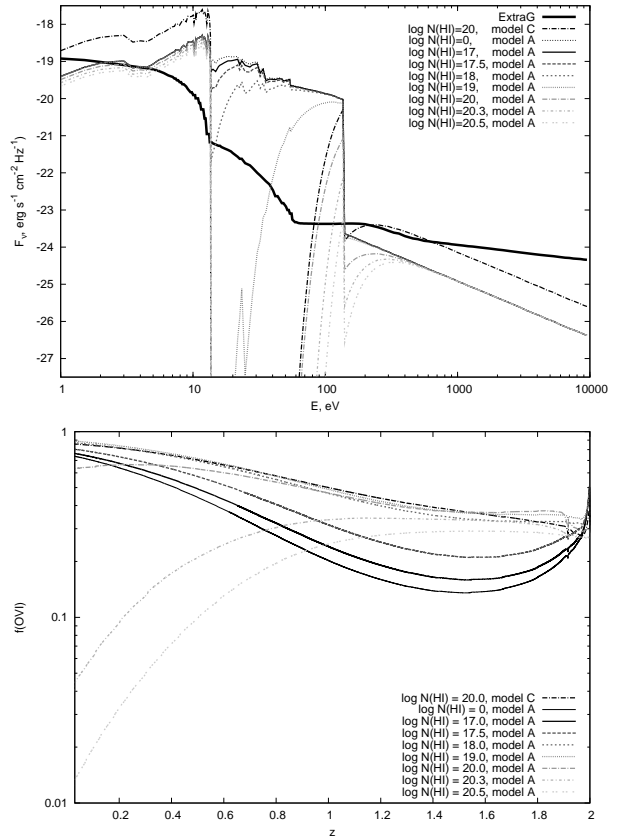


Figure 6. The galactic part of the spectrum in model A at distance $d = 100$ kpc and redshift $z = 0.1$ for several values N_{HI} (upper panel), and the evolution of OVI fraction in gas exposed to this radiation field (lower panel). The thick black line on the upper panel shows the extragalactic part of the spectrum. Redshift dependence of the fraction of OVI ions on the lower panel for different column densities on lower panel shows a catastrophic change at $N_{\text{HI}} > 10^{20} \text{ cm}^{-2}$ with a heavily depressed $f(\text{OVI})$ at lower z . The ratio $N_{\text{HI}}/N_{\text{HeI}} = 10$ is assumed.

around 110-130 eV results in OVI fraction as high as 0.6-0.8. Higher HI column density in underlying galactic discs, $N_{\text{HI}} \gtrsim \text{several} \times 10^{20} \text{ cm}^{-2}$, heavily erases galactic flux in the range $E \sim 110 - 130$ eV, which, for instance in Model A becomes lower than the extragalactic background and the effect of an enhanced OVI fraction vanishes.

3.3 Stability against spectral variations at $\lesssim 91 \text{ \AA}$

It is obviously clear from discussion in Section 3.2 that the enhanced OVI fraction is mainly due to the excess of galactic photons with $E > 113$ eV in the bump at $E \sim 90 - 136$ eV. This bump maintains the OVI fraction at high level and keeps them against recombination to lower ionic states. The left border of this spectral feature, formed by to strong absorption of the galactic ionizing radiation in the disc, is irrelevant from the point of view of the maintainance of OVI – even in the absence of any absorption it remains enhanced (see Figure 6). The right edge of the bump is, however, artificial in origin: as a matter of fact, the cut at 136 eV (91 Å) is a choice of the developers of stellar population codes (e.g. PEGASE, Starburst99, Galaxev). Therefore, in the follow-

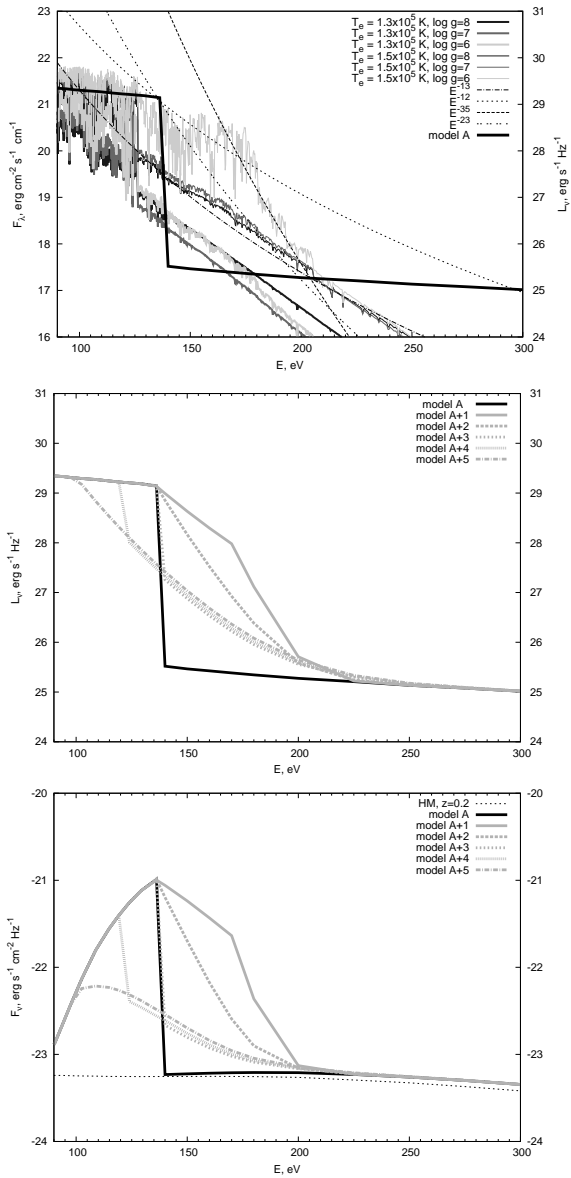


Figure 7. *Upper panel:* Stellar spectra for $T_e = 1.3 \times 10^5$ K (thick grey) and 1.5×10^5 K (thin grey lines) for surface gravity $g = 10^8$, 10^7 and 10^6 cm s^{-2} (dark grey, grey and light grey lines) at solar metallicity taken from the stellar library calculated by Rauch (2003) are shown by grey lines (the left axis). The galactic spectral luminosity accepted in model A is depicted by thick black line (the right axis). Several power-law functions $f_\nu \sim E^{-\alpha}$ are shown for comparison. *Middle panel:* The spectral luminosity in models A (black line) and A+1..A+5 at $z = 0.2$, corresponding to different power-law index α as shown by grey lines. *Bottom panel:* The cumulative ionizing background flux at a distance from the galaxy $d = 100$ kpc and redshift $z = 0.2$ in models A, A+1..A+5 (thick lines), the extragalactic ionizing background (thin dotted line). Models C+1, C+2, ... are defined as the model C with the spectra accepted for models A+1, A+2, ..., correspondingly.

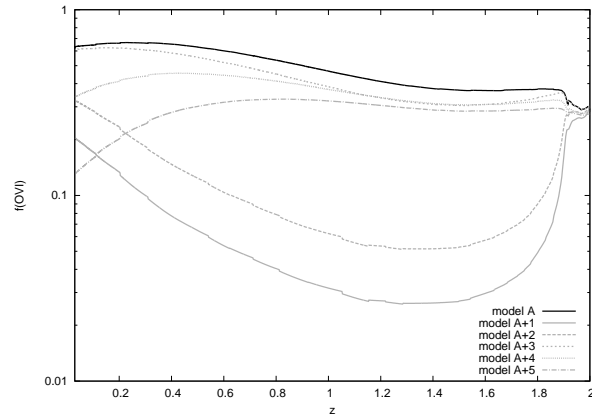


Figure 8. The OVI fraction in gas at a distance $d = 100$ kpc from the galaxy exposed to the spectra corresponding to models A, A+1..A+5.

ing we discuss convergence of our results against possible galactic spectral variations at energy higher than 136 eV.

Extreme ultraviolet and soft X-ray photons ($E \gtrsim 100$ eV) can be produced by post-AGB stars before entering the white dwarf cooling phase (e.g. Werner et al. 1997). During this very bright evolution phase lasting $\lesssim 10^5$ yrs the effective temperature may reach more than $T_e \sim 10^5$ K, while the surface gravity varies as $g \sim 10^{5.5}$ to 10^9 cm s^{-2} . Figure 7 (upper panel) presents the two spectra for $T_e = 1.3 \times 10^5$ K and 1.5×10^5 K for solar metallicity taken from the stellar library (Rauch 2003)². It is seen that the amount of photons with $E \gtrsim 136$ eV increases when the surface gravity g decreases from 10^7 to 10^6 cm s^{-2} for $T_e = 1.5 \times 10^5$ K. On the other hand even a small decrease of effective temperature results in a shortage of photons with $E \gtrsim 125$ eV independent on g . The majority of observed post-AGB stars is known to have masses below $0.6 M_\odot$ and temperatures $T_e \sim 10^5$ to 1.5×10^5 K (e.g. Werner et al. 1997), thus falling into the range shown here. For several spectra a break around $E \sim 125$ eV is clearly seen. One can think that in order to conservatively account this break in stellar population codes the value 136 eV (91 Å) was chosen as an upper limit of energy in their stellar library. It is clearly seen though that even the spectra with a break at $E \sim 125$ eV continue up to $E \sim 150 - 170$ eV and do not show such a strong decrease of flux at $E \gtrsim 136$ eV as used in our calculations. One can think that this gradually decreasing flux above $E \sim 125$ eV produces qualitatively similar effects as does the flux with the break at $E \gtrsim 136$ eV.

In order to check this tentative conclusion we performed calculations of ionic composition for several models of the ionizing flux above 136 eV we construct several spectra and test the appearance of enhanced OVI fraction. We smooth the spectra calculated in PEGASE code at energies $E \sim 100 - 200$ eV and match them at $E \gtrsim 200$ eV to the spectrum obtained from the “ $L_X - SFR$ ” relation as described in Section 2.3 (see Gilfanov et al. 2004). We proceed in the manner that the resulting spectrum would

² This is up to now the most complete library which contains spectra up to 1 Å for hot compact stars.

be qualitatively close to the spectra depicted in the upper panel. Figure 7 (middle panel) shows these spectra normalized on the spectral luminosity in model A. We calculate the ionization and thermal evolution of gas exposed to a cumulative spectrum which includes the extragalactic and the galactic radiation field. Figure 7 (bottom panel) presents an example of the cumulative ionizing background flux at a distance $d = 100$ kpc from the galaxy in models A, A+1..A+5 located at a redshift $z = 0.2$ (thick lines). Figure 8 shows evolution of OVI fraction in gas exposed to the ionizing flux as in models A, A+1..A+5. It is readily seen that in all A+ models the OVI fraction is greater than 0.1 at redshifts $z \lesssim 0.2$. The OVI fraction is several times lower than in model A, but this is still obviously higher than $\lesssim 0.03$, which establishes in gas exposed only to the extragalactic radiation (compare to the dot-dot line for $\log N(\text{HI})=20.5$ in lower panel of Figure 6). In models A+1 and A+2 oxygen at $z \gtrsim 1$ is mainly locked in OVII ions. Starting from $z \sim 1$ the ionization production rate of OVII ions decreases such that recombinations become efficient to replenish lower ionization states, and as a result the fraction of OVI increases at $z < 1$ substantially: from ~ 0.03 at $z = 1.5$ to 0.15 in A+1 and $\gtrsim 0.3$ in A+2 at $z \lesssim 0.2$. This balance between OVII and OVI is kept then quasi-steady down to $z \sim 0$. At large distances the contribution from galactic photons decreases resulting in a higher fraction of OVI in models A+1 and A+2. Note that contrary to models A+1 and A+2 the flux in model A+5 is low and oxygen accumulates mostly in OIV-OV states.

Higher galactic luminosities presented in a set of models C and C+3..C+5, result in a higher OVI fraction: $f(\text{OVI}) \gtrsim 0.5$ in gas located at $d = 100$ kpc at $z \lesssim 0.2$. However, in models C+1 and C+2 the ionization flux at $E \gtrsim 125$ eV is excessive and the fraction of OVI decreases to 0.03 and 0.07 at $z = 0.2$, and reaches only 0.05 and 0.1, at $z = 0$. At larger distances from a galaxy where the flux drops models C+1 and C+2 show an increase of OVI fraction: e.g., in model C+1 it increases to ~ 0.07 (0.11) at 150 kpc and ~ 0.1 (0.17) at 200 kpc at $z = 0.2$ ($z = 0$).

It is readily seen thus that in the majority of these models OVI fraction remains high and reaches $\gtrsim 0.2$ at distance $d \gtrsim 100$ kpc from a galaxy located at $z \lesssim 0.2$. This is more than an order of magnitude higher than can be reached in gas exposed only to the extragalactic radiation at $z \lesssim 0.2$. In model C+1 the OVI fraction reaches 0.1 only for $d \gtrsim 150$ kpc ($z \lesssim 0.2$), while at closer distances most of oxygen is confined into OVII. It is worth stressing though that the model C+1 can be considered as a model with an extreme possible contribution from post-AGB stars, in the sense that models with harder spectrum are unlikely (e.g. Werner et al. 1997), thus one can expect that within conservative models of galactic X-ray spectrum the effect of enhanced OVI remains stable.

3.4 OVI in galactic haloes

In the previous section we have found that OVI fraction can reach high values of $f(\text{OVI}) \sim 0.4 - 0.9$ under the action of ionizing radiation from the underlying galactic stellar population along with the extragalactic radiation field. Such OVI fraction is at least an order higher than the maximum ~ 0.1 reached in commonly used models with gas ionized

collisionally and/or by the extragalactic radiation. Assuming the spherical symmetry and using the time-dependent OVI radial distribution around a host galaxy one can find the OVI column densities along the line of sight crossing the galactic halo at impact parameter b . We integrate from $r = 50$ kpc to 300 kpc.

Figure 9 (upper panel) presents the dependence of $N(\text{OVI})$ on impact parameter b in a $Z = 0.1Z_{\odot}$ isochoric gas within the models A and C. The OVI column density ranges from $N(\text{OVI}) \sim 10^{14.9}$ to $\sim 10^{15.7}$ cm^{-2} at the impact parameter $b \lesssim 200$ kpc – a factor of 3-10 higher than observed by Tumlinson et al. (2011). Therefore circumgalactic gas of an order of magnitude lower metallicity $Z = 0.01Z_{\odot}$ would provide good agreement with observations as shown in Figure 10 (upper panel). It is worth noting though that spatial distribution of metals in circumgalactic environment is highly nonhomogeneous (e.g. Simcoe et al. 2006; Dedikov & Shchekinov 2004), and it is most likely for metals to be locked in clumps of smaller covering factor resulting in a proportional decrease of the column density.

Figure 9 (middle and lower panels) show the column density of OVI in isobaric gas with the initial density 10^{-4} and 5×10^{-5} cm^{-3} , respectively. Isobaric regime is supported by radiation losses and heating from ionizing radiation. Photo-heating grows at large distances from the galaxy, $r \gtrsim 250$ kpc where contribution from OVI ions to cooling decreases. At lower distances OVI fraction increases and it becomes a dominant coolant resulting in a rather efficient cooling. Consequently, column densities grow under isobaric compression: $N(\text{OVI})$ can reach $\sim 10^{15.5-15.9}$ cm^{-2} for the initial density 10^{-4} cm^{-3} , and $\sim 10^{15-15.6}$ cm^{-2} for 5×10^{-5} cm^{-3} . Similarly to the isochoric case gas with lower metallicity ($0.01 Z_{\odot}$) fits observational data better.

Such high column densities are reached for galactic spectra with a cut at 91 Å (see footnote in Section 3.1). In reality though galactic spectra do not show such sharp breaks. In Section 3.3 we considered galactic spectra approximated smoothly around $\sim 100 - 300$ eV to account possible variations of contribution from post-AGB stars. We have found that in the low redshift range, $z \lesssim 0.2$, OVI fraction in gas exposed to such approximated spectra remains sufficiently high in the majority of models considered here. In all cases we have a considerable (an order of magnitude) excess of the column densities calculated in models A, C and with respect to the observed ones as seen in Figure 9).

Tumlinson et al. (2011) have argued that the circumgalactic medium can be a significant reservoir of the ejected material from galaxies. In order to explain large column densities of OVI observed in the haloes they have had to assume that the circumgalactic gas has nearly solar metallicity. This assumption meets though difficulties because the minimum oxygen mass in the halo obtained within such an assumption reaches around 10-70% of the total oxygen mass in the ISM (Tumlinson et al. 2011), which requires in turn unprecedentedly high mass exchange between the galactic ISM disk and a huge circumgalactic reservoir extending up to 150 kpc. Higher OVI fraction obtained in our model reduces the estimates to a more reasonable level, and as a consequence weakens constraints on the sources of oxygen in underlying galaxies.

Contrary, an order of magnitude lower metallicity results in a more consistent scenario of metal production and

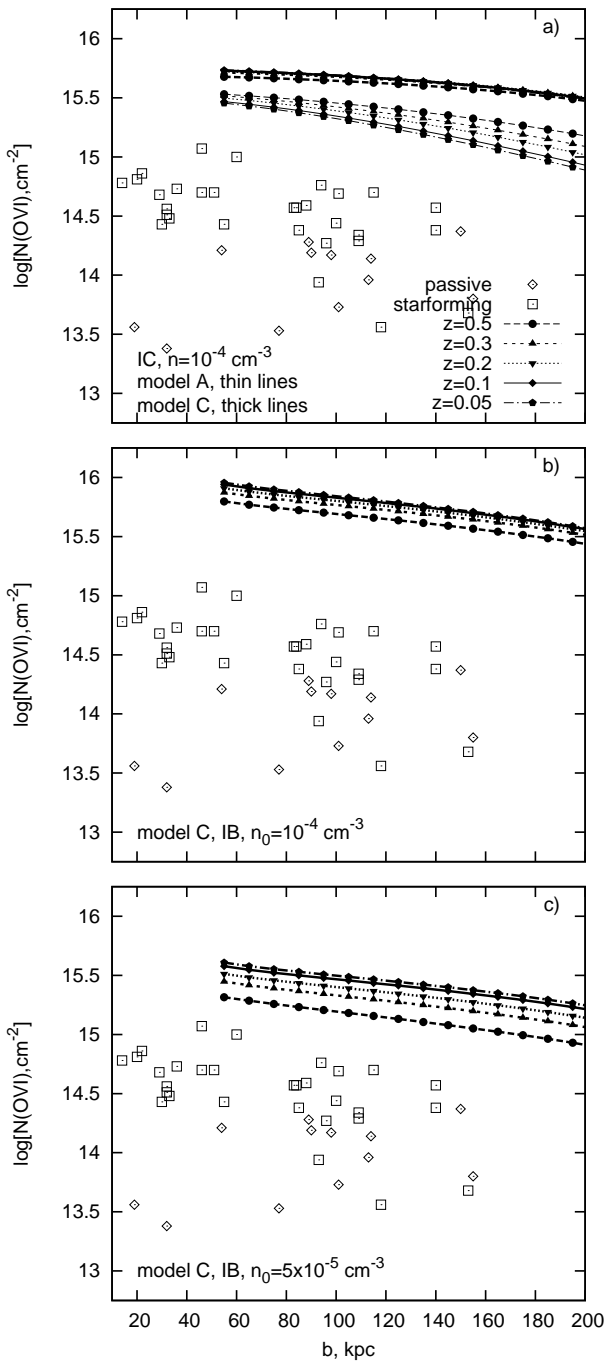


Figure 9. The dependence of the OVI column density on the impact parameter. Thin and thick lines correspond to models A and C (small symbols), respectively. Lines with filled symbols present the dependence for different redshift (see details on the upper panel). The upper panel depicts the column density for isochoric (IC) gas with volumetric density $n = 10^{-4} \text{ cm}^{-3}$, the middle and lower panels show the column density for the isobaric (IB) regime with the initial density 10^{-4} cm^{-3} and $5 \times 10^{-5} \text{ cm}^{-3}$, respectively; the metallicity is $0.1 Z_{\odot}$. Open rhombs and squares depict the observed column densities in the passive and starforming galaxies, correspondingly (Tumlinson et al. 2011); integration is over $r = 50 \text{ kpc}$ to 300 kpc , different symbols correspond to different redshifts.

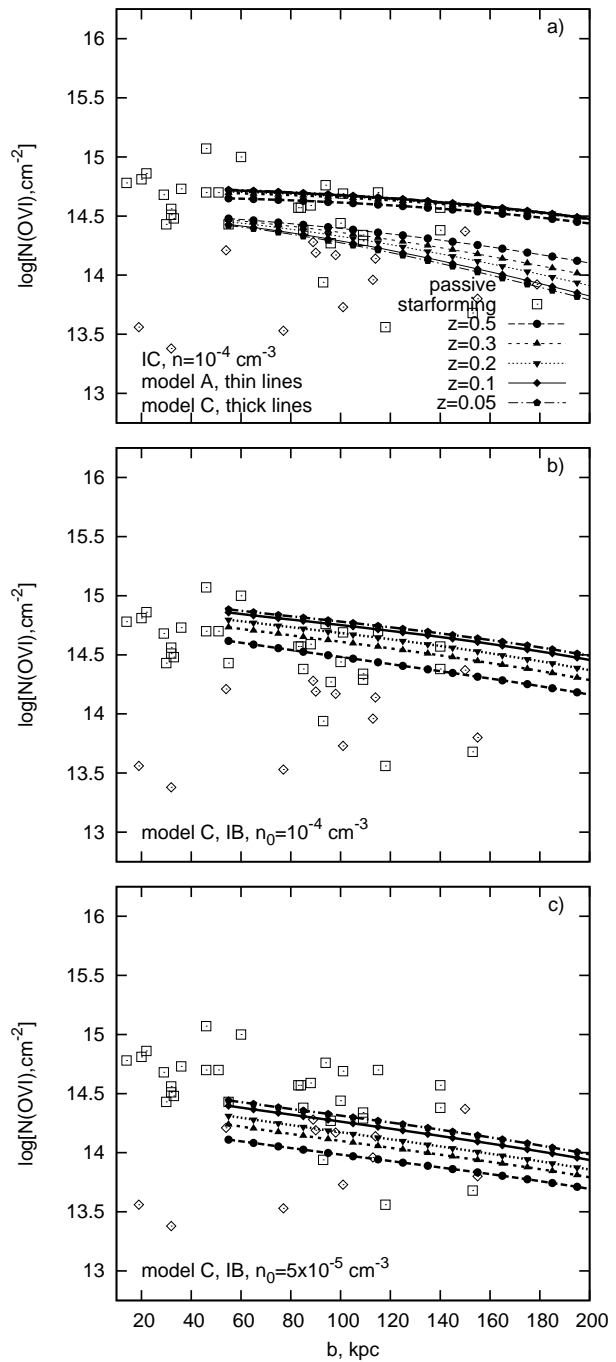


Figure 10. The same as in Figure 9, but for gas metallicity $0.01 Z_{\odot}$.

mass exchange between galactic and circumgalactic gas. Indeed, the total mass of the circumgalactic gas in OVI haloes within $\lesssim 300 \text{ kpc}$ is about $(3-4) \times 10^{10} M_{\odot}$ independent on redshift as estimated from HI data (Prochaska et al. 2011; Steidel, et al. 2010). If such gas would be enriched to the metallicity as high as $0.1 Z_{\odot}$, then the oxygen mass in it equals $\sim 2 \times 10^7 M_{\odot}$. This amount can be produced during a 0.2 Gyr period in a galaxy with $\text{SFR} \sim 6 M_{\odot}/\text{yr}$ (as in our model A), with $0.015 M_{\odot}$ of oxygen returned to the ISM per each $1 M_{\odot}$ star formed (e.g., Thomas et al. 1998). This timescale is significantly shorter than the whole period

of the evolution – several Gyrs, and comparable to the initial period of evolution in our models with the SFR kept nearly constant (upper panel on Figure 1). Because of the high SFR during initial several hundreds Myrs, gas can be ejected from the disk with velocities $\gtrsim 100$ km/s sufficient to reach ~ 100 kpc in approximately 1 Gyr. We assumed throughout that metals are homogeneously distributed in a spherical layer between 50 and 300 kpc. This can be an overestimate, because in general the volume occupied by ejected metals depends on the galaxy mass and for dwarf galaxies can be smaller (e.g. Ferrara et al. 2000). Moreover, metals are locked most likely into small-size dense fragments (e.g. Simcoe et al. 2006), where radiative cooling is efficient. It can result in a rapid cooling and compression and make such fragments to escape detection. Dwarf satellites may add metals in the halo, though their contribution is apparently small because of low metallicity in their ISM: $< 0.1 Z_{\odot}$ (e.g., Salvadori & Ferrara 2009; Ryabova & Shchekinov 2011) and massive dwarfs are rare (e.g., Koposov et al. 2008).

3.5 OVI in galactic haloes: photoequilibrium

In extended galactic haloes gas with a low density, $\sim 10^{-5} - 10^{-3} \text{ cm}^{-3}$, is exposed to rather a high ionizing background consisting of galactic and extragalactic components. Under such conditions the ionic state may reach photoequilibrium³. Ionic composition under photoequilibrium is calculated with making use the CLOUDY. We assume the time-dependent ionizing background described in Section 2.3. The difference between our calculations and the ones performed by Tumlinson et al. (2011), is that besides the Haardt-Madau extragalactic radiation field used in (Tumlinson et al. 2011) we add the galactic contribution, which as we showed above may have crucial consequences: the excess of photons with $E \sim 13.6 - 130$ eV from the underlying stellar population competes the extragalactic radiation, while X-ray photons in the excess with $E > 113$ eV substantially enhance OVI fraction (Section 3.2).

For the fiducial column densities $N_{\text{HI}} = 10^{20} \text{ cm}^{-2}$ and $N_{\text{HeI}} = 10^{19} \text{ cm}^{-2}$ OVI fraction in photoequilibrium is several magnitudes smaller than in our time-dependent models. In photoequilibrium oxygen is mainly locked in less ionized states, OIV-OV, and OVI column density drops to $10^{12.5-13} \text{ cm}^{-2}$. When N_{HI} and N_{HeI} decrease the fraction of OVI instead increases. Even for $N_{\text{HI}} = 5 \times 10^{19} \text{ cm}^{-2}$ (here $N_{\text{HI}}/N_{\text{HeI}} = 10$ is assumed) the OVI column density reaches $\sim 10^{14.2-14.7} \text{ cm}^{-2}$ at the impact distances $b = 50 - 200$ kpc and $z = 0.1$. Further decrease of N_{HI} results in OVI fraction to grow up to $\sim 0.4 - 0.8$, and consequently in higher OVI column densities.

Figure 11 presents the dependence of the OVI column density on the impact parameter for photoequilibrium model with $N_{\text{HI}} = 3 \times 10^{19} \text{ cm}^{-2}$ and time-dependent model with $N_{\text{HI}} = 10^{20} \text{ cm}^{-2}$. The clearly seen considerable difference between photoequilibrium and time-dependent models originates from a well-known fact that gas under nonequilibrium conditions is overionized with respect to

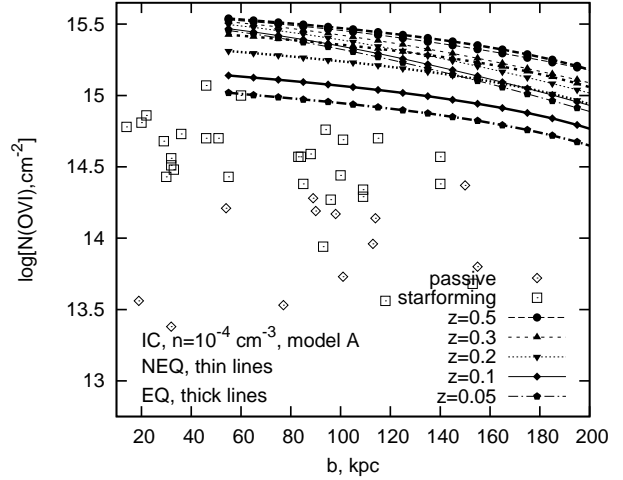


Figure 11. The dependence of the OVI column density on the impact parameter for isochoric gas exposed to the ionizing spectrum in model A. In the photoequilibrium $N_{\text{HI}} = 3 \times 10^{19} \text{ cm}^{-2}$, whereas in time-dependent model $N_{\text{HI}} = 10^{20} \text{ cm}^{-2}$ is adopted ($N_{\text{HI}}/N_{\text{HeI}} = 10$ is assumed). Thin and thick lines correspond to nonequilibrium and photoequilibrium, respectively; density and metallicity are $n = 10^{-4} \text{ cm}^{-3}$ and $0.1 Z_{\odot}$, the other notations are as in Figure 9.

what occurs under equilibrium (e.g. Gnat & Sternberg 2007; Suchkov & Shchekinov 1984; Vasiliev 2011). When N_{HI} decreases, the absorption of galactic ionizing radiation falls down and the peak in the spectrum around $\sim 80 - 130$ eV grows. At such conditions photoionization time shortens, $t_p \sim h\nu/(F_{\nu}\sigma_{\nu}\Delta\nu)$, and the ionic composition approaches photoequilibrium. At low z the extragalactic flux decreases: for example, for $z = 0.1$ $F_{\nu} \sim 3 \times 10^{-24} \text{ erg s}^{-1} \text{ cm}^{-2} \text{ Hz}^{-1}$ at ~ 100 eV (Figure 6). As a result the photoionization timescale t_p of OVI ions increases up to several hundreds Myr, here $\sigma_{\nu} \sim 10^{-18} \text{ cm}^{-2}$ and $\nu/\Delta\nu \sim 10$ are assumed; $\nu = 113.9$ eV is the OVI ionization potential and $\Delta\nu$ is the width of the peak between 113-136 eV. This is about several times shorter than the recombination time for gas with $n = 10^{-4} \text{ cm}^{-3}$ making nonequilibrium effects important.

Smaller absorption in the galactic disc provides higher galactic ionizing flux and shorter photoionization timescale such that ionic composition shifts to photoequilibrium. Thus, nonequilibrium effects are important for OVI ionization kinetics in the circumgalactic gas with $n \gtrsim 10^{-4} \text{ cm}^{-3}$ at $z \lesssim 0.5$. It is therefore can be concluded that the main factor which provides high OVI column densities in massive starforming galaxies at low and moderate metallicities is the excess of photons with energies 113-130 eV from the stellar population of a host galaxy.

4 CONCLUSIONS

In this paper we have presented the photoequilibrium and nonequilibrium (time-dependent) ionization and thermal state of circumgalactic gas located at distances up to $\sim 50 - 300$ kpc around starforming galaxies, and exposed to both extragalactic and galactic time-dependent ionizing background. For the extragalactic background we considered the spectra obtained by Haardt & Madau (2001). Us-

³ The analysis, when collisions become significant compared to photoionization, is out of scope of this paper, details can be found in (Vasiliev 2011)

ing the PEGASE code (Fioc & Rocca-Volmerange 1997) we have calculated chemical and spectro-photometric evolution of galaxies, and have chosen the two models, whose specific star formation rate ($sSFR = SFR/M_*$) and stellar masses are close to the starforming galaxies with large OVI column densities observed in Tumlinson et al. (2011).

We have found that

- the maximum OVI fraction can reach $\sim 0.4 - 0.9$ under physical conditions (gas density and metallicity, and the spectrum shape), which are typical in haloes of starforming galaxies; such a high OVI fraction is due to galactic photons with $E \gtrsim 113$ eV; the effect of enhanced OVI remains stable within conservative models of galactic X-ray spectrum fluctuations at $E \sim 100 - 200$ eV;

- due to such high fraction of OVI its column density ranges in $N(\text{OVI}) \sim 10^{14.9-15.7} \text{ cm}^{-2}$ even for a low metallicity $Z = 0.1Z_\odot$, and $\sim 10^{14-15} \text{ cm}^{-2}$ for $Z = 0.01Z_\odot$ at impact parameters up to $\lesssim 200$ kpc; this results in several times more conservative estimate of the oxygen mass in haloes compared to $M_O = 1.2 \times 10^7 (0.2/f_{\text{OVI}}) M_\odot$ (Tumlinson et al. 2011).

- we have shown therefore that the large OVI column densities observed in haloes of starforming galaxies (Tumlinson et al. 2011) can be found in circumgalactic conditions with nearly 0.01-0.1 of solar metallicity, and correspondingly the requirements to the sources of oxygen in the extended haloes become reasonably conservative.

High OVI column densities in haloes of starforming galaxies can emerge under photoequilibrium as well as under nonequilibrium conditions. The main source is a high radiation flux of photons with $E \gtrsim 113$ eV from the stellar population of starforming galaxies. Nonequilibrium effects for OVI ionization kinetics are important in the circumgalactic environment with $n \gtrsim 10^{-4} \text{ cm}^{-3}$ at $z \lesssim 0.5$.

Very recently Lehner et al. (2014) have reported about high OVI column densities in the circumgalactic medium at $z \sim 2 - 3$ with $N(\text{OVI})$ reaching $\sim 10^{15} \text{ cm}^{-2}$; the observational sample includes absorbers of different type: from Lyman limit to damped Ly α systems. From our point of view such a high OVI column density can be due to the excess of galactic ionizing photons with $E \sim 113 - 135$ eV over the extragalactic background, while the metallicity might be rather low.

5 ACKNOWLEDGEMENTS

We thank Jason Tumlinson for providing data and discussion, and the anonymous referee for valuable comments and pointing to a mistake. This work is supported by the RFBR through the grants 12-02-00365, 12-02-00917, 12-02-92704, and by the Russian Federal Task Program "Research and operations on priority directions of development of the science and technology complex of Russia for 2009-2013" (state contracts 14.A18.21.1304, 2.5641.2011 and 14.A18.21.1179). EV is grateful for support from the "Dynasty" foundation.

REFERENCES

Anderson M.E. & Bregman J.N., 2010, ApJ, 714, 320

- Asplund, M., Grevesse, N., & Sauval, A. J. 2005, in ASP Conf. Ser. 336, Cosmic Abundances as Records of Stellar Evolution and Nucleosynthesis, ed. T. G. Barnes III & F. N. Bash (San Francisco: ASP), 25
- Bregman J.N., Canizares C. R., Cen R., de Herder J-W., Bonamente M. et al. , 2009, Astro2010: The Astronomy and Astrophysics Decadal Survey, Science White Papers, no. 24, arXiv:0906.4984
- Brown P. N., Byrne G. D., & Hindmarsh A. C., 1989, SIAM J. Sci. Stat. Comput., 10, 1038
- Cowie L. L., Songaila A., Kim T.-S., & Hu E. M. 1995, AJ, 109, 1522
- Dedikov S.Yu., Shchekinov Yu.A., 2004, Astr. Rep., 48, 9
- D'Odorico V., Calura F., Cristiani S., & Viel M. 2010, MNRAS, 401, 2715
- Drake J. J. & Testa P., 2005, Nature, 436, 525
- Faucher-Giguère C.-A., Lidz A., Zaldarriaga M., Hernquist L., 2009, ApJ 703, 1416
- Feldmann R., Hooper D., Gnedin N.Y., 2013, ApJ, 763, 21
- Ferrara A., Pettini M., Shchekinov Yu.A., 2000, MNRAS, 319, 539
- Ferland G. J., Korista K. T., Verner D. A., Ferguson J. W., Kingdon J. B. & Verner E. M. 1998, PASP, 110, 761
- Fioc M. & Rocca-Volmerange B., 1997, A&A, 326, 950
- Gilfanov M., Grimm H.-J., Sunyaev R., 2004, MNRAS, 347, L57
- Gnat O. & Sternberg A., 2007, ApJS, 168, 213
- Grevech J. & Putman M.E., 2009, ApJ, 696, 385
- Haardt F. & Madau P., 2001, in Clusters of Galaxies and the High Redshift Universe Observed in X-rays, ed. D. M. Neumann & J. T. V. Tran, astro-ph/0106018
- Hammer F., Puech M., Chemin L., Flores H., Lehnert M.D., 2007, ApJ, 662, 322
- Izotov Yu.I. & Thuan T.X., 1998, ApJ, 500, 188
- Kewley L.J., Dopita M.A., Sutherland R.S., Heisler C.A., Trevena J., 2001, ApJ, 556, 121
- Koposov S., et al. 2008, ApJ, 686, 279
- Lehner N., et al. 2014, ApJ, 788, 119, arXiv:1401.1811
- Pettini M, 1999, in the Proceedings of the ESO Workshop 'Chemical Evolution from Zero to High Redshift'. Eds. J. R. Walsh, M. R. Rosa. Berlin: Springer-Verlag, p. 233
- Prochaska J.X., Weiner B., Chen H.-W., Mulchaey J.S., Cooksey K.L., 2011, ApJ, 740, 91
- Rauch T., 2003, A&A, 403, 709
- Ryabova M.V. & Shchekinov Yu.A., 2011, Ast. Rep., 55, 577
- Quilis V. & Moore B., 2001, ApJ, 555, L95
- Salvadori S., Ferrara A., 2009, MNRAS Lett., 395, 6
- Savaglio S., 2009, *in*: Chemical Abundances in the Universe, K. Cunha, M. Spite & B. Barbuy, eds., IAU Symp No 265
- Schimminovich D. et al. 2007, ApJSS, 173, 315
- Simcoe R.A., Sargent W.L.W., Rauch M., Becker G., 2006, ApJ, 637, 648
- Stanimirović S., Dickey J.M. Krćo M. & Brooks A.M., 2002, ApJ, 576, 773
- Steidel C.C., et al. 2010, ApJ, 717, 289
- Suchkov A. A., Shchekinov Yu. A., 1984, SvAL, 10, 13
- Thomas D., Greggio L., Bender R., 1998, MNRAS, 296, 119
- Tumlinson J. et al. 2011, Science, 334, 948
- Vasiliev E. O., 2011, MNRAS, 414, 3145

- Weiner B.J. & Williams T.B., 1996, *AJ*, 111, 1156
Werner K. et al. 1997, *Rev. Mod. Astron.*, 10, 219
Wiersma R., Schaye J., Smith B.D., 2009, *MNRAS*, 393,
99